

1      **Estimating the impact of a major hurricane on**  
2      **transport processes**

3      Thomas Dobbelaere, Emmanuel Hanert

4      February 22, 2021

5      **Abstract**

6      In most hydrodynamic model studies, currents and waves are simu-  
7      lated separately. This is especially true for the simulation of passive  
8      drifters, whose trajectories are often computed based solely on cur-  
9      rents. Although this simplification holds for most situations, as the  
10     force exerted by waves on currents can be neglected in fair weather  
11     conditions, it may lead to significant errors in storm conditions, during  
12     which local currents are strongly influenced by wind-generated waves.  
13     In this study, current-wave interactions in heavy-wind conditions are  
14     studied by coupling the unstructured-mesh hydrodynamic model SLIM  
15     with the wave model SWAN in the Florida Reef Tract during Hurricane  
16     Irma (Sep. 2017). This coupled model successfully reproduced both  
17     the observed wave behavior and storm surge during the hurricane.  
18     The modeled currents were then used to simulate the trajectories of  
19     passive drifters during the passage of the hurricane. Our results show  
20     that taking wave force into account induces variations of up 1 m/s in  
21     modelled currents on the continental shelf break as well as in the vicin-  
22     ity of reefs and islands. Wave-current interactions can therefore deflect  
23     the trajectories of drifting material by up to 10 km on the passage of  
24     the storm **Add something?**. These results strongly advocate for the  
25     inclusion of wave forces while studying transport processes (sediments,  
26     pollutants, larvae, etc.) under storm conditions

<sup>27</sup> **1 Introduction**

<sup>28</sup> Wave-current interactions in coastal areas are of great importance for coastal  
<sup>29</sup> engineering as they play a key role in sediment transport, morphological  
<sup>30</sup> evolution and pollutant mixing (Bever and MacWilliams, 2013; Li and Johns,  
<sup>31</sup> 1998). However, these interactions are highly nonlinear and can vary sig-  
<sup>32</sup> nificantly in space and time (Wu et al., 2011). Wave-induced currents are  
<sup>33</sup> generated by wave radiation gradients (Longuet-Higgins, 1970), affecting  
<sup>34</sup> water levels near shorelines and wave breaking points (Longuet-Higgins and  
<sup>35</sup> Stewart, 1964), while changes in water levels and currents, in turn, affect the  
<sup>36</sup> motion and evolution of waves (Sikirić et al., 2013). Coupled wave-current  
<sup>37</sup> models are therefore required to capture these complex interactions.

<sup>38</sup> As coastal oceans are characterized by local complex geometries with  
<sup>39</sup> islands, inlets and estuaries, unstructured (usually two-dimensional) mod-  
<sup>40</sup> els are preferred as structured grid models show limitations in resolving  
<sup>41</sup> topologically controlled nearshore processes (Wu et al., 2011; Chen et al.,  
<sup>42</sup> 2007). The effect of wave-interactions becomes even more significant in  
<sup>43</sup> the case of hurricanes, that generate large wind-waves and disturb ocean  
<sup>44</sup> conditions (Liu et al., 2020) by causing coastal upwellings on continental  
<sup>45</sup> shelves (Smith, 1982) and inducing strong currents, waves and storm surges  
<sup>46</sup> in nearshore and coastal regions (Dietrich et al., 2010; Weisberg and Zheng,  
<sup>47</sup> 2006). South Florida and the Gulf of Mexico are particularly vulnerable to  
<sup>48</sup> hurricanes (Malmstadt et al., 2009) and modelling studies predict tropical  
<sup>49</sup> cyclones to increase both in frequency and intensity in this region (Mar-  
<sup>50</sup> sooli et al., 2019; Knutson et al., 2010). Being able to accurately model  
<sup>51</sup> wave-current interactions in this area becomes thus critical.

<sup>52</sup> Individual-based modelling of particulates has been extensively used to  
<sup>53</sup> study the transport of drifting materials such as pollutants, sediments or  
<sup>54</sup> larvae (Garcia-Pineda et al., 2020; Liubartseva et al., 2018; Figueiredo et al.,  
<sup>55</sup> 2013; Frys et al., 2020). Although some of these studies take the impact  
<sup>56</sup> of waves into account by adding Stokes drift velocity, *i.e.* the net drift of a  
<sup>57</sup> floating particle in the direction of the wave propagation (Van Den Bremer  
<sup>58</sup> and Breivik, 2018), to the Eulerian currents, they usually neglect the wave-  
<sup>59</sup> induced currents. Such practice is reasonable in the case of fair weather,  
<sup>60</sup> when wave-induced forces exerted on currents are relatively smaller, but

61 might lead to significant inaccuracies during storm conditions. To assess  
62 the importance of wave-current interactions during a tropical cyclone, we  
63 investigated the transport of drifting particulates on the Florida shelf during  
64 Hurricane Irma, one of the strongest and costliest tropical cyclones on  
65 records in the Atlantic Basin (Chen et al., 2007), that made landfall in Florida  
66 in September 2017.

67 In this study, we developed an unstructured coupled wave-current model of  
68 South Florida to simulate the ocean circulation during hurricane Irma. Both  
69 modelled currents and waves were validated against field measurements  
70 and were then used to simulate the transport of drifting material in the  
71 Florida Keys and the Florida inner shelf during the storm. Model outputs  
72 were then compared with uncoupled simulation results in order to assess  
73 the impact of wave-induced forces and Stokes drift on the modelled currents  
74 and transports.

## 75 **2 Methods**

### 76 **2.1 Study area and data**

77 Large-scale ocean circulation around South Florida is dominated by the  
78 Florida Current (FC), which originates from the Loop Currents (LC) where it  
79 enters the Florida Straits from the Gulf of Mexico, and, downstream, forms  
80 the Gulf Stream. The FC is a major western boundary current character-  
81 ized by spatial variability and meandering, associated with the presence  
82 of cyclonic eddies between the core of the current and the complex reef  
83 topography of the Florida Reef Tract (FRT) (Lee et al., 1995; Kourafalou and  
84 Kang, 2012). The northern half of these reefs are made of early Holocene  
85 reef frameworks and indurated sand ridges while the southern part (the  
86 Florida Keys) is composed of a chain of limestone islands, fossilized rem-  
87 nants of ancient coral reefs and sand bars (Hoffmeister and Multer, 1968;  
88 Shinn, 1988; Lidz and Shinn, 1991). The variability of the FC extends over  
89 a large range of spatial and temporal scales, with periods of 30-70 days in  
90 the Lower Keys (Lee et al., 1995) and shorter periods of 2-21 days in the  
91 Upper Keys (Lee and Mayer, 1977), and exhibits significant seasonal and  
92 interannual cycles (Johns and Schott, 1987; Lee and Williams, 1988; Schott

93 et al., 1988). Circulation on the West Florida Shelf (WFS) on the other hand  
94 is forced by local winds and tidal fluctuations (Lee and Smith, 2002; Liu and  
95 Weisberg, 2012).

96 Field observations were used to validate our model outputs. Modelled sea  
97 surface elevation was validated against tide gauge measurements from  
98 the National Oceanic and Atmospheric Administrations (NOAA) Tides and  
99 Currents dataset. These measurements were taken at four locations: two  
100 in the Florida Keys (Key West and Vaca Key); one on the eastern coast  
101 of Florida (Key West); and one on the western coast (Naples). Currents  
102 were validated against ADCP measurements from the University of South  
103 Florida's College of Marine Science's (USF/CMS) Coastal Ocean Monitoring  
104 and Prediction System (COMPS) for the WFS (Weisberg et al., 2009). More  
105 specifically, we used measurements from moorings C10, C12 and C13,  
106 respectively located at the 25, 50, and 50 m isobaths of the WFS (Liu  
107 et al., 2020). Finally, validation of modelled wave parameters was performed  
108 against four buoy measurements from NOAA's National Data Buoy Center  
109 (NDBC): two on Florida's Eastern shelf and two on the WFS. The locations  
110 of all measurement stations are shown on Fig. 1

## 111 **2.2 Wind and atmospheric pressure for Hurricane Irma**

112 Irma made landfall in Florida on 10 September 2017 as a category 3 storm,  
113 first at Cudjoe Key (Florida Keys) and later on Marco Island, south to Naples  
114 (see hurricane track in Fig. 1). It then weakened to a category 2 storm as it  
115 moved further inland (Pinelli et al., 2018). The storm caused damages to  
116 up to 75% of the buildings at his landfall point in the Florida Keys, making  
117 it one of the strongest and costliest hurricanes on record in the Atlantic  
118 basin (Xian et al., 2018; Zhang et al., 2019). The strongest reported wind  
119 speed was 50 m/s on Marco Island while the highest recorded storm surge  
120 was 2.3 m, although larger wind speed likely occurred in the Florida Keys  
121 (Pinelli et al., 2018) In order to reproduce the wind profile of Irma in our  
122 model, high-resolution H\*Wind (Powell et al., 1998) wind fields were used.  
123 As these data represent 1-min averaged wind speeds, we multiplied them by  
124 a factor 0.93 to obtain 10-min averaged wind speeds (Harper et al., 2010),  
125 more consistent with the time step of our model. Furthermore, H\*Wind

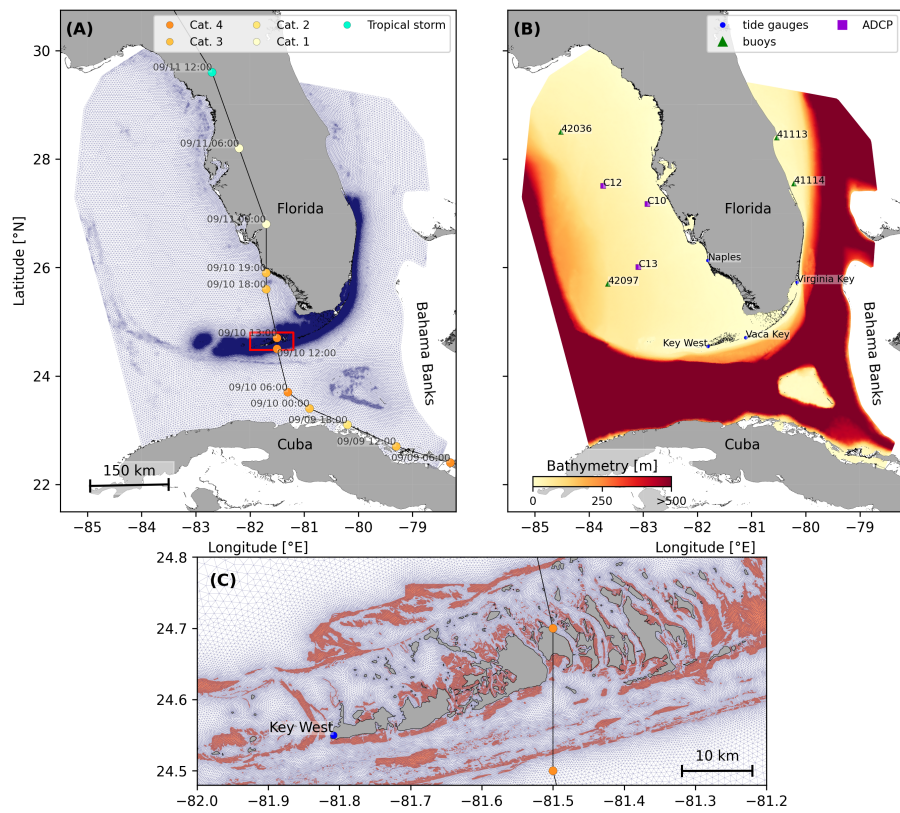


**Fig. 1:** **(A)** Mesh of the computational domain with the trajectory of Irma, category of the hurricane is given by the Saffir-Simpson color scale. **(B)** Bathymetry of the domain with the location of stations used for the validation of the model outputs. **(C)** Close up view of the Lower Keys area, where the mesh resolution reaches 100m near reefs (shown in coral) and islands (highlighted in dark grey)

126 wind profiles did not cover the whole model extent during the hurricane and  
 127 were thus blended within coarser wind field extracted from ECMWF ERA-5  
 128 datasets. Pressure fields of Irma were also constructed using ERA-5 data.  
 129 However, the coarse resolution of the data set caused the depression at the  
 130 center of the hurricane to get smoothed out, leading to an underestimation of  
 131 the pressure gradient in our model. To better capture the central depression  
 132 of Irma, we built a hybrid pressure field using the position and the minimal  
 133 pressure of the core of the hurricane based on its track in the HURDAT  
 134 2 database (Landsea and Franklin, 2013). Based on this information, the  
 135 hybrid pressure field was constructed by combining an idealized Holland  
 136 pressure profile (Lin and Chavas, 2012) within the radius of maximum  
 137 wind speed of Irma (Knaff et al., 2018) with ERA-5 pressure field. The  
 138 transition between from the Holland profile to ERA-5 data outside the radius  
 139 of maximum wind speed data was performed using a smooth step function.

## 140 **2.3 Hydrodynamic model**

141 Ocean currents generated during hurricane Irma around South Florida were  
 142 modelled using the 2D barotropic version of the unstructured-mesh coastal  
 143 ocean model SLIM<sup>1</sup>. The model mesh covers an area similar to the model  
 144 extent of Dobbelaere et al. (2020b), that includes the FRT but also the  
 145 Florida Strait and part of the Gulf of Mexico (Figure 1). However, this area  
 146 has been slightly extended northeastward and westward in order to include  
 147 the NOAA-NDBC buoys. Furthermore, in order to withstand potential cell  
 148 drying due to storm conditions in this study, we solved the conservative  
 149 shallow water equations with wetting-drying, that write:

$$\begin{aligned}
 \frac{\partial H}{\partial t} + \nabla \cdot (\mathbf{U}) &= 0 \\
 \frac{\partial \mathbf{U}}{\partial t} + \nabla \cdot \left( \frac{\mathbf{U}\mathbf{U}}{H} \right) &= -f \mathbf{e}_z \times \mathbf{U} + \alpha g H \nabla(H - h) - \frac{1}{\rho} \nabla p_{\text{atm}} + \frac{1}{\rho} \boldsymbol{\tau}_s \quad (1) \\
 &\quad + \nabla \cdot (\nu \nabla \mathbf{U}) - \frac{C_b}{H^2} |\mathbf{U}| \mathbf{U} + \gamma (\mathbf{U}_* - \mathbf{U})
 \end{aligned}$$

150 where  $H$  is the water column height and  $\mathbf{U}$  is the depth-averaged transport;  
 151  $f$  is the Coriolis coefficient;  $g$  is the gravitational acceleration;  $h$  is the

---

<sup>1</sup><https://www.slim-ocean.be>

152 bathymetry;  $\alpha$  is a coefficient stating whether the mesh element is wet  
 153 ( $\alpha = 1$ ) or dry ( $\alpha = 0$ );  $\nu$  is the viscosity;  $C_b$  is the bulk bottom drag  
 154 coefficient;  $\nabla p_{\text{atm}}$  is the atmospheric pressure gradient;  $\tau_s$  is the surface  
 155 stress due to wind; and  $\gamma$  is a relaxation coefficient towards a reference  
 156 transport  $U_*$ . As in Frys et al. (2020) and Dobbelaere et al. (2020b), SLIM  
 157 currents were gradually relaxed towards HYCOM (Chassignet et al., 2007) in  
 158 regions where the water depth exceeds 50m.

159 At very high wind speeds, the white cap is blown off the crest of the waves,  
 160 which generates a layer of droplets that acts as a slip layer for the winds  
 161 at the ocean-atmosphere interface (Holthuijsen et al., 2012). This causes  
 162 a saturation of the wind drag coefficient for strong winds (Donelan et al.,  
 163 2004; Powell et al., 2003). To account for the impact of this saturation  
 164 on the surface wind stress in our model, we implemented the wind drag  
 165 parameterization of Moon et al. (2007). In this parameterization, the drag  
 166 coefficient  $C_d$  depends on the wind speed at 10-m height  $U_{10}$  according to:

$$C_d = \kappa^2 \log \left( \frac{10}{z_0} \right)^{-2} \quad (2)$$

167 where  $\kappa$  is the von Karman constant. The roughness length  $z_0$  in Eq. 2 is a  
 168 function of the 10-m wind speed  $U_{10}$ , whose expression writes:

$$z_0 = \begin{cases} \frac{0.0185}{g} U_*^2 & \text{if } U_{10} \leq 12.5 \text{ m/s} \\ [0.085(-0.56U_*^2 + 20.255U_* + 2.458) - 0.58] \times 10^{-3} & \text{if } U_{10} > 12.5 \text{ m/s} \end{cases} \quad (3)$$

169 with  $U_*$  the friction velocity. The relation between  $U_{10}$  and  $U_*$  is given by:

$$U_{10} = -0.56U_*^2 + 20.255U_* + 2.458 \quad (4)$$

170 The mesh resolution depends on the distance to coastlines and reefs follow-  
 171 ing the approach of (Dobbelaere et al., 2020b). The mesh was then further  
 172 refined as a function of bathymetry and bathymetry gradient, in order to  
 173 satisfy SWAN refinement criterion<sup>2</sup>  $h/A \geq a$ , where  $h$  is the water depth  
 174 and  $A$  is the element area. This criterion improves the efficiency of the

---

<sup>2</sup><http://swanmodel.sourceforge.net/unswan/unswan.htm>

175 computational grid by locally increasing the mesh resolution in areas where  
 176 the bathymetry or evolution of the waves change rapidly while avoiding to  
 177 invest too many computational resources where the physics or depth change  
 178 less. The mesh was generated using the Python library seamsh<sup>3</sup>, based  
 179 on the the open-source mesh generator GMSH (Geuzaine and Remacle,  
 180 2009) and is composed of approximately  $7.7 \times 10^5$  elements. The coarsest  
 181 elements, far away from the FRT, had a characteristic length size of about 5  
 182 km whereas the finest elements had a characteristic length of 100 m near  
 183 coastlines and reefs (Fig 1).

## 184 **2.4 Wave model**

185 Waves were modelled using parallel unstructured SWAN (Booij et al., 1999)  
 186 on the same mesh as SLIM. This model solves the action balance equation,  
 187 which reads (Mei, 1989):

$$\frac{\partial N}{\partial t} + \nabla_x \cdot [(c_g + \mathbf{u})N] + \frac{\partial}{\partial \theta}[c_\theta N] + \frac{\partial}{\partial \sigma}[c_\sigma N] = \frac{S_{in} + S_{ds} + S_{nl}}{\sigma} \quad (5)$$

188 where  $N = E/\sigma$  is the wave action density;  $\theta$  is the wave propagation  
 189 direction;  $\sigma$  is the wave relative frequency;  $c_g$  is the wave group velocity,  
 190  $\mathbf{u} = \mathbf{U}/H$  is SLIM depth-averaged current velocity;  $c_\theta$  and  $c_\sigma$  are the propa-  
 191 gation velocities in spectral space due to refraction and shifting in frequency  
 192 due to variations in depth and currents; and  $S_{in}$ ,  $S_{ds}$ , and  $S_{nl}$  respectively  
 193 represent wave growth by wind, wave decay and nonlinear transfers of  
 194 wave energy through interactions between triplets and quadruplets. Spectra  
 195 were discretized with 48 direction bins and 50 frequency bins logarithmically  
 196 distributed from 0.3 to 2 Hz. Exponential wind growth was parameterized  
 197 using the formulation of Janssen (1991), while dissipations by whitecapping  
 198 and bottom dissipations followed the formulations of Komen et al. (1984)  
 199 and Madsen et al. (1989) respectively. Coefficients for exponential wind  
 200 growth and whitecapping parameterizations were based on the results of  
 201 Siadatmousavi et al. (2011), that significantly differ from SWAN's default  
 202 settings. Formulation of Komen et al. (1984) is used by default by SWAN  
 203 for wind energy input while default parameters for whitecapping [wait for  
 204 zenobe to be back]. The choice of these formulations was motivated by

---

<sup>3</sup><https://pypi.org/project/seamsh/>

205 the appearance of numerical instabilities in the region of the Gulf Stream  
 206 using SWAN's default parameter values. Finally, wave boundary conditions  
 207 were derived from WAVEWATCH III (Tolman et al., 2009) spectral outputs at  
 208 buoy locations. Surface wave induce a net drift in te direction of the wave  
 209 propagation, known as Stokes drift (Van Den Bremer and Breivik, 2018;  
 210 Stokes, 1880). This net drift has significant impacts on sediment motion  
 211 in near shore regions (Hoefel and Elgar, 2003), the formation of Langmuir  
 212 cells (Langmuir, 1938; Craik and Leibovich, 1976) as well as the transport of  
 213 heat, salt or pollutants such as oil or micro-plastic in the upper ocean layer  
 214 (McWilliams and Sullivan, 2000; Röhrs et al., 2012; Drivedal et al., 2014).  
 215 To model adequately the Stokes profile in mixed wind-driven sea and swell  
 216 conditions, the full two- dimensional wave spectrum must be represented  
 217 by a spectral wave model within a wave-current coupling (Van Den Bremer  
 218 and Breivik, 2018). In this study, depth-averaged Stokes drift was therefore  
 219 computed by SWAN using the following formula:

$$\mathbf{u}_s = \int_0^{2\pi} \int_0^{+\infty} \frac{\sigma^3}{h \tanh(2kh)} E(\sigma, \theta) (\cos \theta, \sin \theta) d\sigma d\theta \quad (6)$$

220 where  $k$  is the norm of the wave vector;  $h$  is the water depth; and  $E(\sigma, \theta)$  is  
 221 the wave energy density.

## 222 2.5 Coupled model

223 SLIM and SWAN are coupled so that they run on the same computational  
 224 core and the same unstructured mesh. SLIM is run first and passes com-  
 225 puted wind velocities ( $\mathbf{U}_{10}$ ), water levels ( $\eta = H - h$ ) and depth-averaged  
 226 currents ( $\mathbf{u} = \mathbf{U}/H$ ) to SWAN, as well as a roughness length ( $z_0$ ) for the bot-  
 227 tom dissipation formulation of Madsen et al. (1989). This roughness length  
 228 is computed from SLIM's bulk drag coefficient  $C_b$  following the approach of  
 229 Dietrich et al. (2011) so that both models have consistent bottom dissipation  
 230 parameterizations. SWAN then utilizes these quantities to compute the wave  
 231 radiation stress gradient, that is then passed to SLIM as the wave-induced  
 232 stress on currents  $\tau_{\text{wave}}$ . SLIM then uses this quantity to update the the  
 233 value of the surface stress  $\tau_s$  in Eq. 1, that now becomes the sum of wind  
 234 and wave-induced stresses  $\tau_s = \tau_{\text{wind}} + \tau_{\text{wave}}$ .

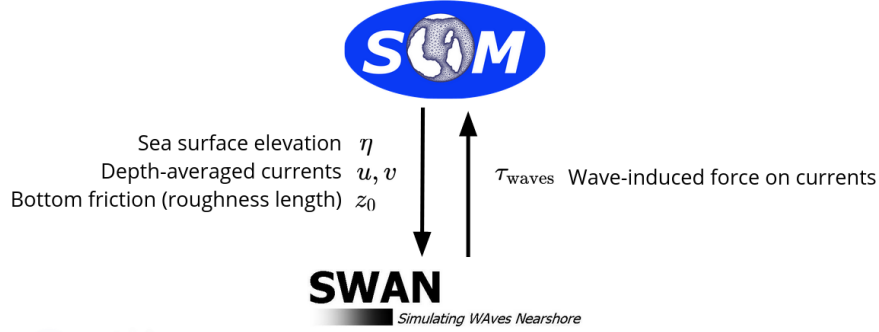


**Fig. 2:** Schematic illustration of the coupled SLIM+SWAN model.

235 SLIM equations are integrated using an implicit scheme while SWAN is  
 236 unconditionally stable (Dietrich et al., 2010), allowing both models to be run  
 237 with relatively large time steps. In this study, both models were therefore  
 238 run sequentially using a time step of 600s, so that each computational core  
 239 was alternating running either SLIM or SWAN. As in the coupling between  
 240 SWAN and ADCIRC (Dietrich et al., 2010), both models utilize the same  
 241 local sub-mesh, allowing for a one-to-one correspondence between the  
 242 geographic locations of the mesh vertices. No interpolation is therefore  
 243 needed when passing computed quantities from a model to another, which  
 244 allows for efficient inter-model communication. However, as SLIM applies  
 245 discontinuous Galerkin finite element methods, an additional conversion step  
 246 to a continuous framework was required to transmit SLIM nodal quantities to  
 247 SWAN.

### 248 3 Results

249 We first validated the reconstructed atmospheric fields of hurricane Irma as  
 250 well the modelled currents and waves of our coupled model against fields  
 251 measurements. Once we had built some confidence in our model accuracy  
 252 we used these, we used these modelled quantities to represent the transport  
 253 of passive particles in the Lower Florida Keys during the passage of the  
 254 hurricane. These transports were obtained using three data sets: (i) currents  
 255 from an uncoupled SLIM simulation of Irma (SLIM); (ii) currents modelled  
 256 by the coupled SLIM+SWAN model (SLIM+SWAN); (iii) currents modelled

257 by the coupled SLIM+SWAN model to which the modelled depth-averaged  
258 Stokes drift was added (Eq. 6) (SLIM+SWAN+Stokes). We then compared  
259 the particle trajectories obtained with these three sets of currents to assess  
260 the impact of wave-current coupling on drifter transport during the passage  
261 of a major hurricane.

### 262 **3.1 Validation**

263 H\*Wind winds and hybrid pressure field agree well with station measure-  
264 ments at Vaca Key station (Fig. 3). The hybrid pressure field shows better  
265 agreement with observations than ERA-5 pressure as it successfully re-  
266 produces the storm depression. ERA-5 fields, on the other hand, fail to  
267 resolve the low pressure at the core of the hurricane due to their coarser  
268 grid, leading to an overestimation of 8 mbar of the storm depression. Both  
269 H\*Wind and ERA-5 agree well with observed wind speeds although both  
270 data sets tend to slightly overestimate the width and intensity of the wind  
271 peak. However, H\*wind profiles show a better match with the timing of the  
272 observed peak, that ERA-5 winds tend to anticipate. H\*wind also exhibits a  
273 slightly narrower peak in wind speed, which better agrees with observations.  
274 Hydrodynamic outputs of the coupled wave-current agree well with tide  
275 gauge and ADCP measurements (Fig. 4). The timing and amplitude of the  
276 storm surges are well reproduced by the coupled model, the largest model  
277 error being an overestimation of 18 cm of the elevation peak at Virginia Key.  
278 The fit is especially good at Naples, where both the positive and negative  
279 surges are captured by the coupled model with a 5 cm accuracy. This  
280 result is of interest as negative surges, although less studied, affect water  
281 exchanges between the estuaries and the coastal ocean and disturb the  
282 benthic ecosystems (Liu et al., 2020). Modelled 2D currents were validated  
283 against depth-averaged ADCP measurements at mooring station C10, C12  
284 and C13 (Fig. 4). As in (Liu et al., 2020), vector correlation analysis (Kundu,  
285 1976) is performed to compare modelled and observed current velocity  
286 vectors. Correlation coefficients ( $\rho$ ) between simulated and observed depth-  
287 averaged currents were 0.84, 0.74 and 0.73 respectively C10, C12 and C13  
288 locations respectively. Average veering angles were computed as well and  
289 were below 12°, as in (Liu et al., 2020). However, in our case, no clear

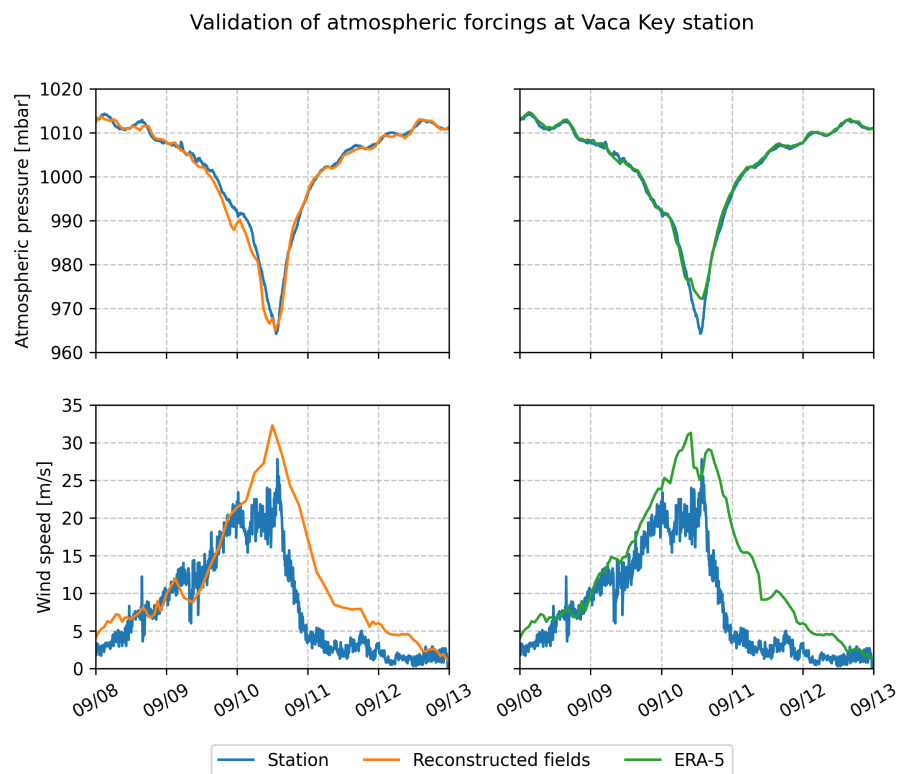


**Fig. 3:** Comparison of reconstructed wind atmospheric pressure with field measurements and coarser ECMWF ERA-5 profiles during Irma. The generated hybrid atmospheric better capture the observed storm depression while H\*wind winds better match the measured peak in wind speed.

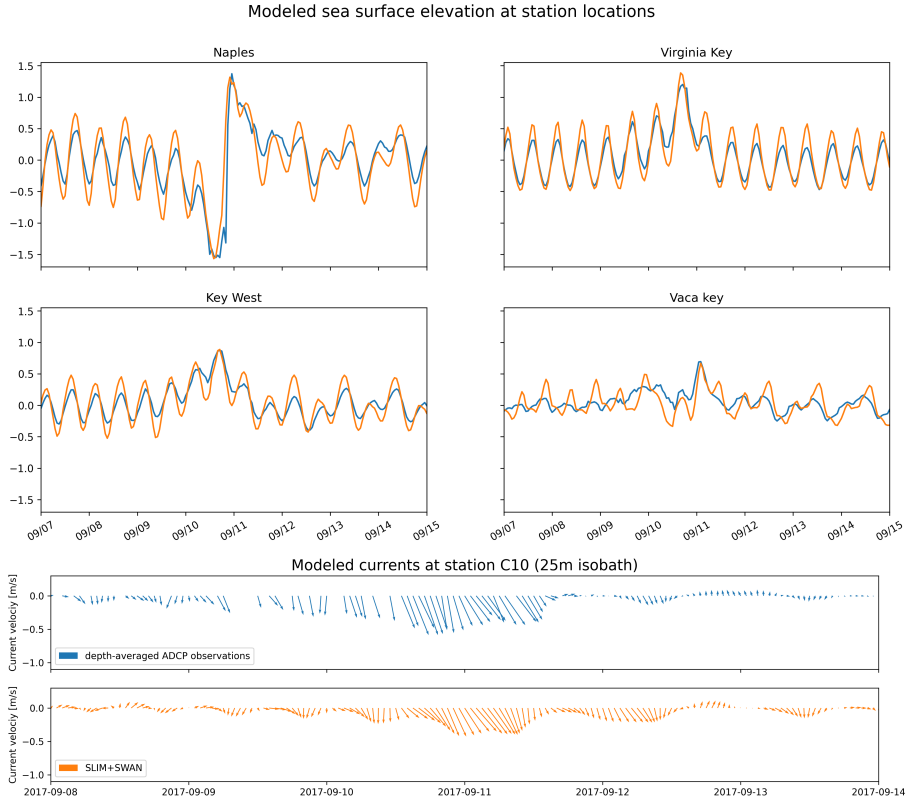


**Fig. 4:** Comparison of modelled sea surface elevation and current velocity with tide gauge measurements and observed velocity at mooring C10 (see Fig. 1 for their location). Timing and amplitudes of the storm surges are well reproduced by the model. Modelled current velocities agree well with observations, with a correlation coefficient of 0.83 and an average veering angle of  $6^\circ$  at mooring C10.

290 tendency regarding modelled current behavior compared to observations

291 was observed. As expected from a depth-averaged model, the best fit with  
292 observations is obtained at the shallowest mooring C10, located on the 25m  
293 isobath, with an average veering angle of  $6^\circ$ .

294 The simulated significant wave height agrees well with observations on the  
295 WFS, where errors on the peak value do not exceed 5%. On the East Florida  
296 Shelf, errors are slightly larger reaching 20%. Although the model outputs  
297 agree well with observations, a lag in significant wave height is observed  
298 for all 4 buoys. Moreover, the peak in significant wave height tends to be  
299 underestimated at buoys 41113 and 41114, located on the East Florida Shelf.

300 Other wave parameters were better reproduced by the model on the WFS as  
301 well, as illustrated for buoy 42036 in Fig. 5. This good fit on the WFS is not  
302 surprising as the parameters used for wind energy input and whitecapping  
303 dissipation were based on the calibration performed by (Siadatmousavi et al.,  
304 2011) on the Northern Gulf of Mexico. Wind-induced wave growth might  
305 therefore be underestimated on the eastern shelf. Consequently, incident  
306 wave do not receive enough energy to grow after breaking on the bank  
307 boundary, leading to an underestimation of the significant wave height at  
308 the location of the buoys. Nonetheless, as this study focused on the wave  
309 produced by Irma, that made landfall on the western coasts of Florida, the  
310 use of parameterizations calibrated for the Gulf of Mexico seems reasonable.

### 311 **3.2 Impact of waves on currents and transport**

312 The impact of hurricane-induced wave-current interactions is first evaluated  
313 by computing the norm of the maximum difference in current velocity be-  
314 tween uncoupled SLIM and coupled SLIM+SWAN model runs during the  
315 passage of Irma through the Florida Keys (from 2017-09-07 to 2017-09-13).  
316 The differences in modelled currents appear to be stronger on the shelf  
317 break and over coral reefs (Fig. 6). These results highlight the significant  
318 impact of wave-induced forces, that can yield differences of up to 1 m/s dur-  
319 ing the hurricane, with stronger currents being obtained with SLIM+SWAN.  
320 This suggests that neglecting wave-current interactions during Irma would  
321 results in a significant underestimation of transport over reefs.  
322 To quantify the impact of these differences in velocity fields, we compared  
323 the trajectories of virtual particles driven by currents produced by SLIM  
324 alone and SLIM+SWAN simulations in the Florida Keys. First, we identified  
325 the areas where the differences between the modelled currents were the  
326 largest. Then, we determined the potential origination regions of particles  
327 reaching these areas on the passage of the hurricane through the Florida  
328 Keys using backtracking methods (Dobbelare et al., 2020a). These regions  
329 are highlighted by the 4 release regions of Fig. 7. Finally, particles were  
330 released from these four regions and advected by currents produced by the  
331 coupled and uncoupled models. At each time step, the center of mass of  
332 the modelled particle clouds were computed. The distance between these

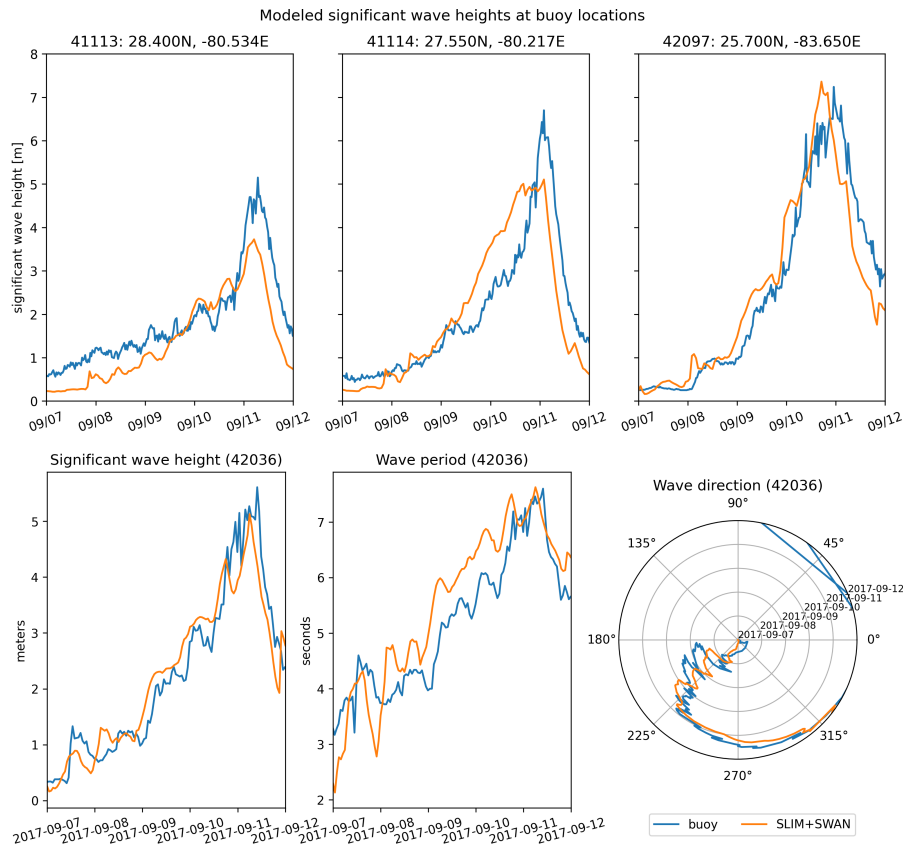


**Fig. 5:** Comparison of modelled wave parameters with observation at buoys location. Modelled significant wave height agrees well with field measurement. As model parameters were calibrated for the Northern Gulf of Mexico, observations are better reproduced at buoys located on the WFS, as illustrated for buoy 42036

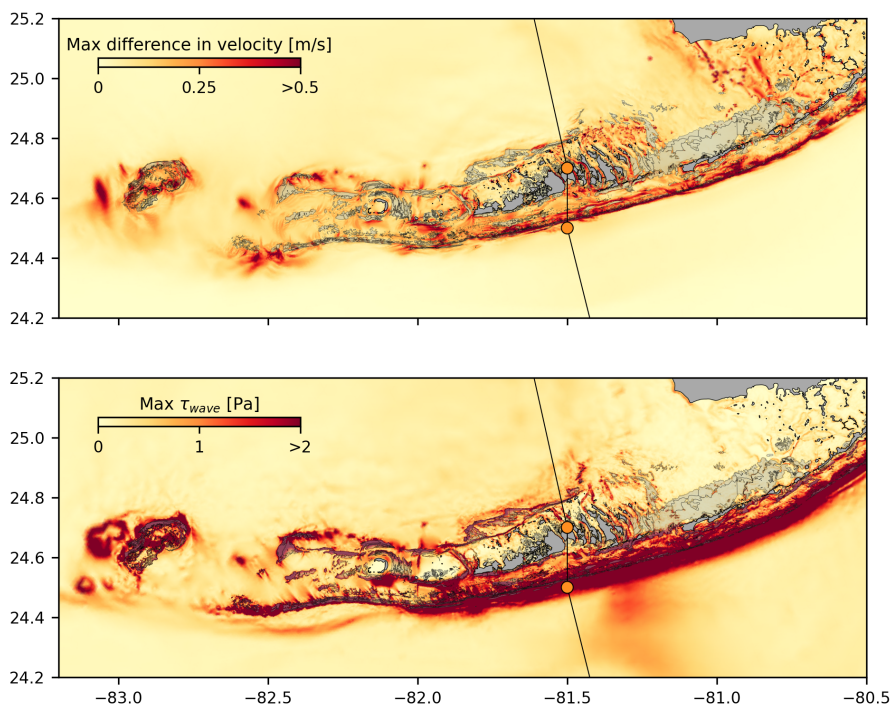


**Fig. 6:** Maximum of the difference between SLIM and SLIM+SWAN currents speed between 2017-09-07 00:00:00 and 2017-09-13 00:00:00. The difference between the coupled and uncoupled model, which represents the effect of the wave-induced stress, can yield differences of 0.5 m/s in the simulated currents during the passage of the hurricane. SLIM+SWAN currents velocities are larger than the currents modeled by SLIM alone. Islands are highlighted in dark grey and coral reefs in lighter grey

333 centers of mass was used as a measure of the impact of the wind-generated  
334 wave coupling on the modelled current in the Florida Keys during hurricane  
335 Irma. This comparison was performed with 3 sets of currents: the currents  
336 modelled by uncoupled SLIM (SLIM); the currents modelled by coupled  
337 SLIM+SWAN (SLIM+SWAN); and the SLIM+SWAN currents with depth-  
338 averaged Stokes drift (SLIM+SWAN+Stokes) [sentence is too condensed].  
339 The results of these comparisons are shown in Fig. 7 [reformulate as active  
340 sentence]. Differences between the modelled trajectories are negligible  
341 before the passage of the hurricanes in the Florida Keys. Then, distance  
342 between the centers of mass of the particles abruptly increase to up to  
343 tens of kilometers as Irma gets through the Keys to finally stabilize after  
344 the passage of the hurricane. These results support the assumption that  
345 wave-induced transport is negligible compared to advection by Eulerian  
346 currents in fair weather conditions. Particles advected by the currents of  
347 the coupled model tend to remain on the shelf while particles advected by  
348 SLIM alone are mostly transported along the shelf break. Although not  
349 shown in this paper, comparison of SLIM and SLIM+SWAN trajectories were  
350 conducted as well. The evolution of the distance between centers of mass  
351 of the particle clouds showed similar trends while yielding smaller values.  
352 Modelled maximal depth-averaged Stokes drift reached up to 0.2 m/s during  
353 the passage of Irma through the Florida Keys. This suggests that both the  
354 impact of wave-induced force on Eulerian currents and Stokes drift should be  
355 taken into account while modelling particle transport under storm conditions.

## 356 4 Discussion and conclusions

- 357 Impact of waves on coral connectivity
- 358 Ability of wave model to correctly capture gradient in significant wave height  
359 due to current-waves interactions under tropical cyclones depends on:
- 360     • Broad perspective  $\Rightarrow$  not limited to FL
- 361     • Mention search and rescue
- 362     • However, ignoring waves in storm conditions could result in significant  
363       inaccuracies in modelled trajectories, as illustrated in the case of

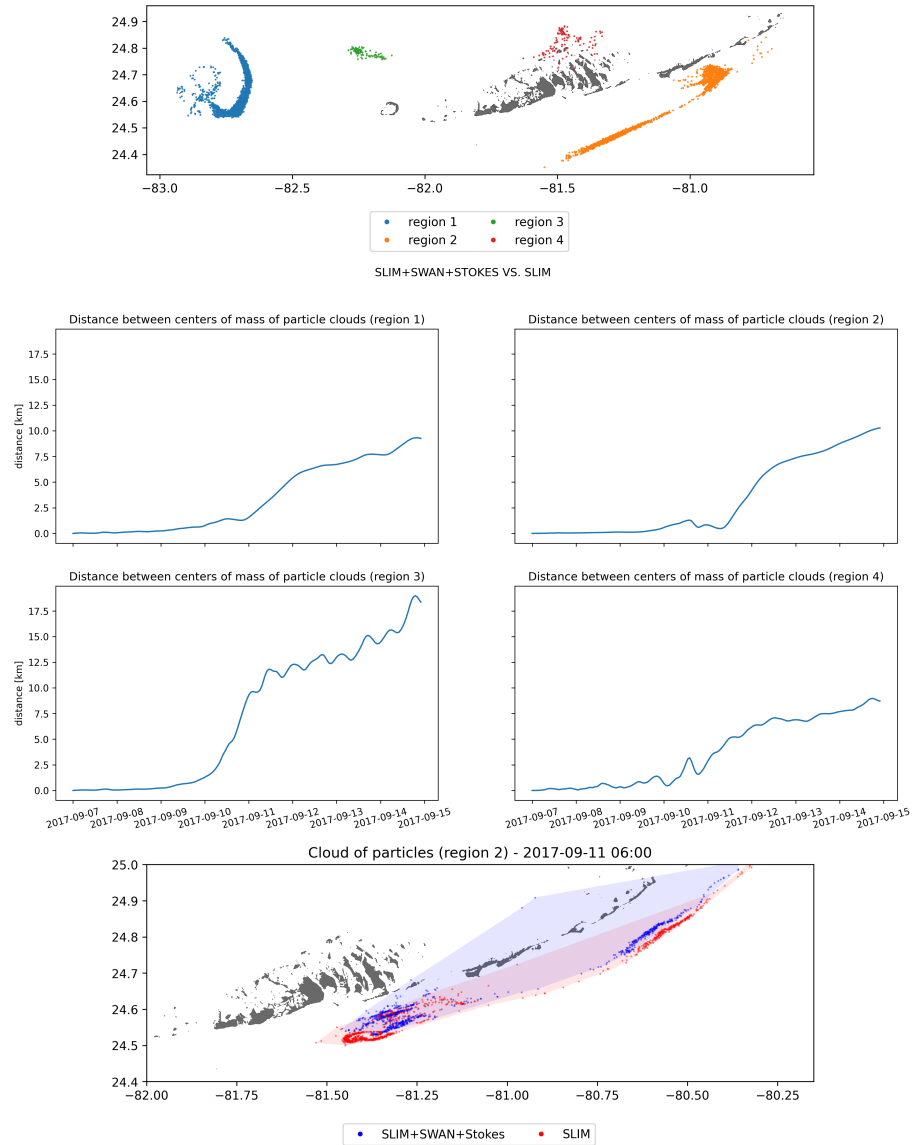


**Fig. 7:** Comparison of passive drifters trajectories with SLIM+SWAN+Stokes drift vs. SLIM alone. A snapshot of the positions of the particles released from region 2 is shown after the passage of Irma in the Florida Keys. Particles advected by the currents of the coupled model tend to remain on the shelf while particles advected by SLIM alone are mostly transported along the shelf break

364 release region 2 in Fig. 7

- 365 • Spatial (10km → 5km) and spectral (36 dir. → 48 dir.) resolution  
366 (Hegermiller et al., 2019)
- 367 • Directional spreading of incident waves (Villas Bôas et al., 2020)

## 368 **Conflict of Interest Statement**

369 The authors declare that the research was conducted in the absence of any  
370 commercial or financial relationships that could be construed as a potential  
371 conflict of interest.

## 372 **Author Contributions**

## 373 **Funding**

## 374 **Acknowledgments**

375 Computational resources were provided by the Consortium des Équipements  
376 de Calcul Intensif (CÉCI), funded by the F.R.S.-FNRS under Grant No. 2.5020.11.  
377 Thomas Dobbelaere is a PhD student supported by the Fund for Research  
378 training in Industry and Agriculture (FRIA/FNRS).

## 379 **Supplementary Material**

380 The Supplementary Material for this article is attached to the submitted  
381 document.

## 382    **References**

- 383    Bever, A. J. and MacWilliams, M. L. (2013). Simulating sediment transport  
384       processes in San Pablo Bay using coupled hydrodynamic, wave, and  
385       sediment transport models. *Marine Geology*, 345:235–253.
- 386    Booij, N., Ris, R. C., and Holthuijsen, L. H. (1999). A third-generation wave  
387       model for coastal regions: 1. Model description and validation. *Journal*  
388       *of geophysical research: Oceans*, 104(C4):7649–7666.
- 389    Chassignet, E. P., Hurlburt, H. E., Smedstad, O. M., Halliwell, G. R., Hogan,  
390       P. J., Wallcraft, A. J., Baraille, R., and Bleck, R. (2007). The HYCOM  
391       (hybrid coordinate ocean model) data assimilative system. *Journal of*  
392       *Marine Systems*, 65(1-4):60–83.
- 393    Chen, C., Huang, H., Beardsley, R. C., Liu, H., Xu, Q., and Cowles, G. (2007).  
394       A finite volume numerical approach for coastal ocean circulation studies:  
395       Comparisons with finite difference models. *Journal of Geophysical*  
396       *Research: Oceans*, 112(C3).
- 397    Craik, A. D. and Leibovich, S. (1976). A rational model for Langmuir circula-  
398       tions. *Journal of Fluid Mechanics*, 73(3):401–426.
- 399    Dietrich, J., Bunya, S., Westerink, J., Ebersole, B., Smith, J., Atkinson,  
400       J., Jensen, R., Resio, D., Luettich, R., Dawson, C., et al. (2010). A  
401       high-resolution coupled riverine flow, tide, wind, wind wave, and storm  
402       surge model for southern Louisiana and Mississippi. part ii: Synoptic  
403       description and analysis of hurricanes Katrina and Rita. *Monthly Weather*  
404       *Review*, 138(2):378–404.
- 405    Dietrich, J., Westerink, J., Kennedy, A., Smith, J., Jensen, R., Zijlema, M.,  
406       Holthuijsen, L., Dawson, C., Luettich, R., Powell, M., et al. (2011).  
407       Hurricane Gustav (2008) waves and storm surge: Hindcast, synoptic  
408       analysis, and validation in southern Louisiana. *Monthly Weather Review*,  
409       139(8):2488–2522.
- 410    Dobbelaere, T., Muller, E., Gramer, L., Holstein, D., and Hanert, E. (2020a).  
411       Report on the potential origin of the SCTLD in the Florida Reef Tract.  
412       Available online at: [https://floridadep.gov/rcp/coral/documents/  
413       report-potential-origin-sctld-florida-reef-tract](https://floridadep.gov/rcp/coral/documents/report-potential-origin-sctld-florida-reef-tract).

- 414 Dobbelaere, T., Muller, E. M., Gramer, L. J., Holstein, D. M., and Hanert, E.  
415 (2020b). Coupled epidemic-hydrodynamic modeling to understand the  
416 spread of a deadly coral disease in Florida. *Frontiers in Marine Science*,  
417 7:1016.
- 418 Donelan, M., Haus, B., Reul, N., Plant, W., Stiassnie, M., Gruber, H., Brown,  
419 O., and Saltzman, E. (2004). On the limiting aerodynamic roughness of  
420 the ocean in very strong winds. *Geophysical Research Letters*, 31(18).
- 421 Drivdal, M., Broström, G., and Christensen, K. (2014). Wave-induced mixing  
422 and transport of buoyant particles: application to the statfjord a oil spill.  
423 *Ocean Science*, 10(6):977–991.
- 424 Figueiredo, J., Baird, A. H., and Connolly, S. R. (2013). Synthesizing larval  
425 competence dynamics and reef-scale retention reveals a high potential  
426 for self-recruitment in corals. *Ecology*, 94(3):650–659.
- 427 Frys, C., Saint-Amand, A., Le Hénaff, M., Figueiredo, J., Kuba, A., Walker, B.,  
428 Lambrechts, J., Vallaeyns, V., Vincent, D., and Hanert, E. (2020). Fine-  
429 scale coral connectivity pathways in the Florida Reef Tract: implications  
430 for conservation and restoration. *Frontiers in Marine Science*, 7:312.
- 431 Garcia-Pineda, O., Androulidakis, Y., Le Hénaff, M., Kourafalou, V., Hole,  
432 L. R., Kang, H., Staples, G., Ramirez, E., and DiPinto, L. (2020). Mea-  
433 suring oil residence time with GPS-drifters, satellites, and Unmanned  
434 Aerial Systems (UAS). *Marine pollution bulletin*, 150:110644.
- 435 Geuzaine, C. and Remacle, J.-F. (2009). Gmsh: A 3-d finite element mesh  
436 generator with built-in pre-and post-processing facilities. *International*  
437 *journal for numerical methods in engineering*, 79(11):1309–1331.
- 438 Harper, B., Kepert, J., and Ginger, J. (2010). *Guidelines for converting*  
439 *between various wind averaging periods in tropical cyclone conditions*.  
440 Citeseer.
- 441 Hegermiller, C. A., Warner, J. C., Olabarrieta, M., and Sherwood, C. R.  
442 (2019). Wave-current interaction between Hurricane Matthew wave  
443 fields and the Gulf Stream. *Journal of Physical Oceanography*,  
444 49(11):2883–2900.

- 445 Hoefel, F. and Elgar, S. (2003). Wave-induced sediment transport and  
446 sandbar migration. *Science*, 299(5614):1885–1887.
- 447 Hoffmeister, J. and Multer, H. (1968). Geology and origin of the Florida Keys.  
448 *Geological Society of America Bulletin*, 79(11):1487–1502.
- 449 Holthuijsen, L. H., Powell, M. D., and Pietrzak, J. D. (2012). Wind and waves  
450 in extreme hurricanes. *Journal of Geophysical Research: Oceans*,  
451 117(C9).
- 452 Janssen, P. A. (1991). Quasi-linear theory of wind-wave generation applied  
453 to wave forecasting. *Journal of physical oceanography*, 21(11):1631–  
454 1642.
- 455 Johns, W. E. and Schott, F. (1987). Meandering and transport variations  
456 of the Florida Current. *Journal of physical oceanography*, 17(8):1128–  
457 1147.
- 458 Knaff, J. A., Sampson, C. R., and Musgrave, K. D. (2018). Statistical tropi-  
459 cal cyclone wind radii prediction using climatology and persistence:  
460 Updates for the western North Pacific. *Weather and Forecasting*,  
461 33(4):1093–1098.
- 462 Knutson, T. R., McBride, J. L., Chan, J., Emanuel, K., Holland, G., Landsea,  
463 C., Held, I., Kossin, J. P., Srivastava, A., and Sugi, M. (2010). Tropical  
464 cyclones and climate change. *Nature geoscience*, 3(3):157–163.
- 465 Komen, G., Hasselmann, S., and Hasselmann, K. (1984). On the exis-  
466 tence of a fully developed wind-sea spectrum. *Journal of physical*  
467 *oceanography*, 14(8):1271–1285.
- 468 Kourafalou, V. H. and Kang, H. (2012). Florida Current meandering and  
469 evolution of cyclonic eddies along the Florida Keys Reef Tract: Are they  
470 interconnected? *Journal of Geophysical Research: Oceans*, 117(C5).
- 471 Kundu, P. K. (1976). Ekman veering observed near the ocean bottom.  
472 *Journal of Physical Oceanography*, 6(2):238–242.
- 473 Landsea, C. W. and Franklin, J. L. (2013). Atlantic hurricane database un-  
474 certainty and presentation of a new database format. *Monthly Weather*  
475 *Review*, 141(10):3576–3592.

- 476 Langmuir, I. (1938). Surface motion of water induced by wind. *Science*,  
477 87(2250):119–123.
- 478 Lee, T. N., Leaman, K., Williams, E., Berger, T., and Atkinson, L. (1995).  
479 Florida Current meanders and gyre formation in the southern Straits  
480 of Florida. *Journal of Geophysical Research: Oceans*, 100(C5):8607–  
481 8620.
- 482 Lee, T. N. and Mayer, D. A. (1977). Low-frequency current variability and  
483 spin-off eddies along the shelf off southeast Florida. *Collected Reprints*,  
484 1(1):344.
- 485 Lee, T. N. and Smith, N. (2002). Volume transport variability through the  
486 Florida Keys tidal channels. *Continental Shelf Research*, 22(9):1361–  
487 1377.
- 488 Lee, T. N. and Williams, E. (1988). Wind-forced transport fluctuations of the  
489 Florida Current. *Journal of Physical Oceanography*, 18(7):937–946.
- 490 Li, Z. and Johns, B. (1998). A three-dimensional numerical model of surface  
491 waves in the surf zone and longshore current generation over a plane  
492 beach. *Estuarine, Coastal and Shelf Science*, 47(4):395–413.
- 493 Lidz, B. H. and Shinn, E. A. (1991). Paleoshorelines, reefs, and a rising sea:  
494 South florida, usa. *Journal of Coastal Research*, pages 203–229.
- 495 Lin, N. and Chavas, D. (2012). On hurricane parametric wind and appli-  
496 cations in storm surge modeling. *Journal of Geophysical Research: Atmospheres*, 117(D9).
- 498 Liu, Y. and Weisberg, R. H. (2012). Seasonal variability on the West Florida  
499 shelf. *Progress in Oceanography*, 104:80–98.
- 500 Liu, Y., Weisberg, R. H., and Zheng, L. (2020). Impacts of hurricane Irma  
501 on the circulation and transport in Florida Bay and the Charlotte Harbor  
502 estuary. *Estuaries and Coasts*, 43(5):1194–1216.
- 503 Liubartseva, S., Coppini, G., Lecci, R., and Clementi, E. (2018). Tracking  
504 plastics in the Mediterranean: 2D Lagrangian model. *Marine pollution  
bulletin*, 129(1):151–162.

- 506 Longuet-Higgins, M. S. (1970). Longshore currents generated by obliquely  
507 incident sea waves. *Journal of geophysical research*, 75(33):6778–  
508 6789.
- 509 Longuet-Higgins, M. S. and Stewart, R. (1964). Radiation stresses in water  
510 waves; a physical discussion, with applications. In *Deep sea research and oceanographic abstracts*, volume 11, pages 529–562. Elsevier.
- 512 Madsen, O. S., Poon, Y.-K., and Gruber, H. C. (1989). Spectral wave  
513 attenuation by bottom friction: Theory. In *Coastal Engineering 1988*,  
514 pages 492–504.
- 515 Malmstadt, J., Scheitlin, K., and Elsner, J. (2009). Florida hurricanes and  
516 damage costs. *southeastern geographer*, 49(2):108–131.
- 517 Marsooli, R., Lin, N., Emanuel, K., and Feng, K. (2019). Climate change  
518 exacerbates hurricane flood hazards along US Atlantic and Gulf Coasts  
519 in spatially varying patterns. *Nature communications*, 10(1):1–9.
- 520 McWilliams, J. C. and Sullivan, P. P. (2000). Vertical mixing by Langmuir  
521 circulations. *Spill Science & Technology Bulletin*, 6(3-4):225–237.
- 522 Mei, C. C. (1989). *The applied dynamics of ocean surface waves*, volume 1.  
523 World scientific.
- 524 Moon, I.-J., Ginis, I., Hara, T., and Thomas, B. (2007). A physics-based  
525 parameterization of air–sea momentum flux at high wind speeds and  
526 its impact on hurricane intensity predictions. *Monthly weather review*,  
527 135(8):2869–2878.
- 528 Pinelli, J.-P., Roueche, D., Kijewski-Correa, T., Plaz, F., Prevatt, D., Zisis,  
529 I., Elawady, A., Haan, F., Pei, S., Gurley, K., et al. (2018). Overview  
530 of damage observed in regional construction during the passage of  
531 Hurricane Irma over the State of Florida. In *Forensic Engineering 2018: Forging Forensic Frontiers*, pages 1028–1038. American Society of  
532 Civil Engineers Reston, VA.
- 534 Powell, M. D., Houston, S. H., Amat, L. R., and Morisseau-Leroy, N. (1998).  
535 The HRD real-time hurricane wind analysis system. *Journal of Wind  
536 Engineering and Industrial Aerodynamics*, 77:53–64.

- 537 Powell, M. D., Vickery, P. J., and Reinhold, T. A. (2003). Reduced drag coefficient for high wind speeds in tropical cyclones. *Nature*, 422(6929):279–283.
- 540 Röhrs, J., Christensen, K. H., Hole, L. R., Broström, G., Drivdal, M., and Sundby, S. (2012). Observation-based evaluation of surface wave effects on currents and trajectory forecasts. *Ocean Dynamics*, 62(10–12):1519–1533.
- 544 Schott, F. A., Lee, T. N., and Zantopp, R. (1988). Variability of structure and transport of the Florida Current in the period range of days to seasonal. *Journal of Physical Oceanography*, 18(9):1209–1230.
- 547 Shinn, E. A. (1988). The geology of the Florida Keys. *Oceanus*, 31(1):46–53.
- 548 Siadatmousavi, S. M., Jose, F., and Stone, G. (2011). Evaluation of two WAM white capping parameterizations using parallel unstructured SWAN with application to the Northern Gulf of Mexico, USA. *Applied Ocean Research*, 33(1):23–30.
- 552 Sikirić, M. D., Roland, A., Janečković, I., Tomazić, I., and Kuzmić, M. (2013). Coupling of the Regional Ocean Modeling System (roms) and Wind Wave Model. *Ocean Modelling*, 72:59–73.
- 555 Smith, N. P. (1982). Response of Florida Atlantic shelf waters to hurricane David. *Journal of Geophysical Research: Oceans*, 87(C3):2007–2016.
- 557 Stokes, G. G. (1880). On the theory of oscillatory waves. *Transactions of the Cambridge philosophical society*.
- 559 Tolman, H. L. et al. (2009). User manual and system documentation of WAVEWATCH III TM version 3.14. *Technical note, MMAB Contribution*, 276:220.
- 562 Van Den Bremer, T. and Breivik, Ø. (2018). Stokes drift. *Philosophical Transactions of the Royal Society A: Mathematical, Physical and Engineering Sciences*, 376(2111):20170104.
- 565 Villas Bôas, A. B., Cornuelle, B. D., Mazloff, M. R., Gille, S. T., and Arduin, F. (2020). Wave–current interactions at meso-and submesoscales: Insights from idealized numerical simulations. *Journal of Physical Oceanography*, 50(12):3483–3500.

- 569 Weisberg, R., Liu, Y., and Mayer, D. (2009). Mean circulation on the west  
570 Florida continental shelf observed with long-term moorings. *Geophys.*  
571 *Res. Lett*, 36:L19610.
- 572 Weisberg, R. H. and Zheng, L. (2006). Hurricane storm surge simulations  
573 for Tampa Bay. *Estuaries and Coasts*, 29(6):899–913.
- 574 Wu, L., Chen, C., Guo, P., Shi, M., Qi, J., and Ge, J. (2011). A FVCOM-  
575 based unstructured grid wave, current, sediment transport model, I.  
576 Model description and validation. *Journal of Ocean University of China*,  
577 10(1):1–8.
- 578 Xian, S., Feng, K., Lin, N., Marsooli, R., Chavas, D., Chen, J., and Hatzikyri-  
579 akou, A. (2018). Brief communication: Rapid assessment of damaged  
580 residential buildings in the Florida Keys after Hurricane Irma. *Natural*  
581 *Hazards and Earth System Sciences*, 18(7):2041–2045.
- 582 Zhang, C., Durgan, S. D., and Lagomasino, D. (2019). Modeling risk of man-  
583 groves to tropical cyclones: A case study of Hurricane Irma. *Estuarine,*  
584 *Coastal and Shelf Science*, 224:108–116.